Applied Surface Science 600 (2022) 154010

Contents lists available at ScienceDirect

Applied Surface Science

journal homepage: www.elsevier.com/locate/apsusc

Full Length Article

Inherent selective pulsed chemical vapor deposition of amorphous hafnium oxide / titanium oxide nanolaminates

Yunil Cho [a], James Huang [b], Christopher F. Ahles [b], Zichen Zhang [b], Keith Wong [d], Srinivas Nemani [d], Ellie Yieh [d], Andrew C. Kummel [c,*]

[a] Electrical and Computer Engineering Program, University of California, La Jolla, San Diego, CA 92093, United States
[b] Materials Science and Engineering Program, University of California, La Jolla, San Diego, CA 92093, United States
[c] Department of Chemistry & Biochemistry, University of California, La Jolla, San Diego, CA 92093, United States
[d] Applied Materials, Inc, Sunnyvale, CA 95054, United States

ARTICLE INFO

Keywords:
Inherent selective Deposition
Selective Amorphous Oxide Deposition
Water-Free Deposition
Nanolaminates
Nanoscale Patterning

ABSTRACT

Water-free Inherent selective pulsed chemical vapor deposition (CVD) of HfO_2/TiO_2 nanolaminates on Si and SiO_2 in preference to SiCOH has been studied. SiCOH is highly porous alkylated SiO_2, which is used as a nonreactive low-k dielectric. $Ti(O^iPr)_4$ [titanium(IV) isopropoxide] and $Hf(O^tBu)_4$ [Hafnium tert butoxide] were used in the CVD study. Previous studies showed that metal alkoxide precursors could form oxide films through thermal decomposition. However, single oxide films greater than 2 nm can be rough due to crystallization. To solve this issue, HfO_2/TiO_2 nanolaminate structures were studied. With sequential dosing of each precursor in a supercycle at 300 °C sample temperature, HfO_2/TiO_2 nanolaminate films with thin (less than 3 nm) sublayers were selectively deposited. The films were smooth with root mean square (RMS) roughness lower than 0.5 nm and almost amorphous from XRD analysis; this is unexpected since both oxides readily crystalize. Amorphous nanolaminate oxide film deposition with high selectivity was achieved by controlling each sublayer thickness and the Hf:Ti ratio. TEM studies proved that ~ 20 nm of the nanolaminate film could also be selectively deposited on nanoscale patterned surfaces. This selective amorphous nanolaminate oxide CVD process has a potential to be applicable in the nanoscale patterning in MOSFET fabrication.

1. Introduction

Atomic layer deposition (ALD) and chemical vapor deposition (CVD) are commonly used in the semiconductor industry.[1] Among various methods, thermal deposition (as opposed to plasma-enhanced deposition) is one of the primary methods for ALD and CVD on three dimensional topologies. Within a specific sample temperature range, also known as the 'ALD window', a self-limiting chemical reaction between the ligands of each precursor occurs, which deposits approximately one atomic level layer on the surface. As the sample temperature increases above the 'ALD window', often self-limiting ALD reactions no longer dominate the deposition, but thermal CVD prevails. At the CVD temperature, the ligands of metal precursor decompose and desorb or form reactive ligands such as hydroxyl (–OH), which promote fast film growth.[2] Due to its self-limiting nature, ALD forms smooth and conformal films. However, with careful control of dosing conditions, CVD can also produce smooth and conformal films.[3]

Nanoscale patterning is a crucial issue in fabricating leading-edge commercial semiconductor devices. The need for novel patterning is acute in backend metallization when metals and dielectric layers with high aspect ratios in nanometer-scale are employed. Area selective oxide deposition in conjunction with the double patterning technique is possible for nanoscale patterning.[2,4] For selective oxide deposition in backend fabrication, water-free deposition is favorable since it can not only induce higher selectivity[5] but also prevent damage of metals and low k dielectric, e.g., SiCOH. There are three methods of selective deposition: inherent selective deposition, selective passivation, and selective activation. The inherent selective deposition is based on reactivity differences of different surfaces during precursor mediated chemisorption. The binding energy difference between precursor and different surface bonds can induce selective deposition on a specific surface.[2,6–9] The inherent selective deposition is advantageous since it does not require additional steps to add or remove passivants. However, the majority of selective depositions are based on selective

* Corresponding author at: Department of Chemistry and Biochemistry, University of California, La Jolla, California, 92093, United States.
E-mail address: akummel@ucsd.edu (A.C. Kummel).

https://doi.org/10.1016/j.apsusc.2022.154010
Received 30 April 2022; Received in revised form 14 June 2022; Accepted 16 June 2022
Available online 24 June 2022
0169-4332/© 2022 Elsevier B.V. All rights reserved.

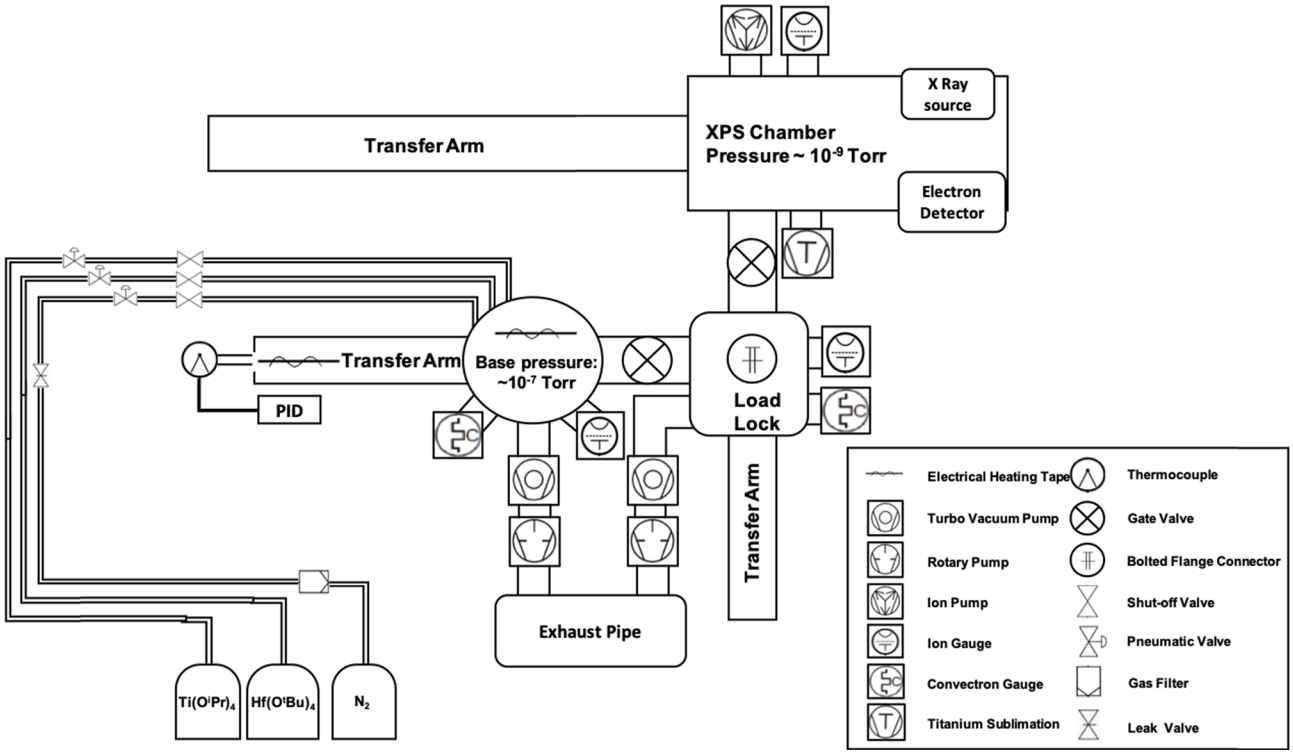

Fig. 1. A schematic of UHV chamber for HfO_2/TiO_2 nanolaminate CVD and XPS analysis. The system consists of three chambers: load lock chamber for sample loading, deposition chamber for CVD process, and UHV XPS chamber for XPS analysis.

passivation. Specific molecules, such as a long-chain alkane, can inhibit the nucleation of precursors. Therefore, by selectively reacting the passivant on a particular surface, selective deposition on surfaces without the passivant occurs with consequent selective ALD/CVD. [10–14] In addition, selective activation, such as electron beam-induced ALD (EEALD), can also induce selective deposition on the pretreated surface.[15–18]

In many cases, thick oxide deposition is desired, including the nanoscale patterning applications. However, previous studies showed that many oxide films, including TiO_2 [2], and HfO_2 [19], crystallize with increasing film thickness. The crystallization is not preferable if a smooth film is required. Making a nanolaminate structure with two or more oxides can solve this issue.[20–26] There have been many studies that nanolaminate structures of different oxide films inhibit crystallization. Al_2O_3 is known to be amorphous regardless of its thickness; therefore, many nanolaminate structures using Al_2O_3 have been studied. [20–23] G. E. Testoni et al. proved that TiO_2 films can stay amorphous by making a nanolaminate structure adding Al_2O_3 monolayers.[20] Testoni et al. showed that even a monolayer of Al_2O_3 between two TiO_2 sublayers could inhibit crystallization. However, it was also shown that crystallization could not be inhibited if each TiO_2 sublayer is more than ~ 3 nm in thickness. The research on nanolaminate structures using two different oxides that are both prone to crystallization has also been studied.[24–26] D. H. Triyoso et al. proved that the nanolaminate structures of HfO_2/TiO_2 can form amorphous films.[24] With an ALD using titanium tetrachloride ($TiCl_4$), hafnium tetrachloride ($HfCl_4$), and water, nanolaminate structures with various Hf:Ti ratios were tested. All films were amorphous and showed lower RMS roughness than pure HfO_2 and TiO_2 films. The drawback of this process is that halogens, e.g., Cl and F, can corrode metals while the H_2O will degrade SiCOH, so the process is incompatible with the middle or back of the line processing. Moreover, most of the research about oxide nanolaminate structures studied the mechanical, electrical, and optical characteristics but not their selective deposition.

The authors previously reported pulsed chemical vapor deposition (CVD) of TiO_2 at around 300 °C with inherent selectivity for deposition on Si or SiO_2, but not on SiCOH, a non-reactive low k dielectric material; ~17 nm and ~ 40 nm of TiO_2 were selectively deposited on Si and SiO_2, respectively, while less than 0.1 nm was deposited on SiCOH.[2] However, the thick TiO_2 film formed nano-crystallites which induced rough surface formation. This roughness needs to be reduced for application to nanoscale patterning. The authors also recently reported selective pulsed CVD of TiO_2/Al_2O_3 and HfO_2/Al_2O_3 nanolaminates by sequential pulses of titanium isopropoxide ($Ti(O^iPr)_4$) / trimethylaluminum (TMA) and hafnium tertbutoxide ($Hf(O^tBu)_4$) / TMA, respectively.[27] Around 20 nm of a nanolaminate film with an RMS roughness lower than 0.5 nm was selectively deposited on Si and SiO_2, in preference to SiCOH. However, as TMA does not contain oxygen, too much TMA dosing (Al richer nanolaminate) could inhibit the film growth.

In the present study, sequential pulsed CVD at 300 °C sample temperature using $Ti(O^iPr)_4$ and $Hf(O^tBu)_4$ to form HfO_2/TiO_2 nanolaminate films was studied. $Hf(O^tBu)_4$ and $Ti(O^iPr)_4$ are metal alkoxide precursors which contain four oxygen atoms per metals atom inside their ligands so that these precursors can solely be used to deposit oxide film by thermal decomposition at 300 °C. This is a unique approach for nanolaminate formation since two oxygen-containing metal precursors were employed; for nanolaminate oxide formation, usually, only one oxygen-containing precursor (ex: H_2O) is employed with two different metal precursors (ex: $TiCl_4$, $HfCl_4$). Success with dual oxygen-containing metal precursors enables a large variety of halogen-free precursors to be employed.

Inherent selectivity of the process was tested on hydrogen-terminated silicon, hydroxyl-terminated SiO_2, and SiCOH. SiCOH was alkyl ($-C_xH_y$) terminated SiO_2 and was used as a non-reactive surface. [28–31] After confirming the selectivity and crystallization in single oxide films, both the amorphousness and selectivity of HfO_2/TiO_2 nanolaminates film were documented. The test was done with three different Hf:Ti ratio nanolaminate films to verify the effect of the selectivity of each single oxide on that of the nanolaminate film. In addition, X-ray diffraction (XRD) was employed to determine the roles

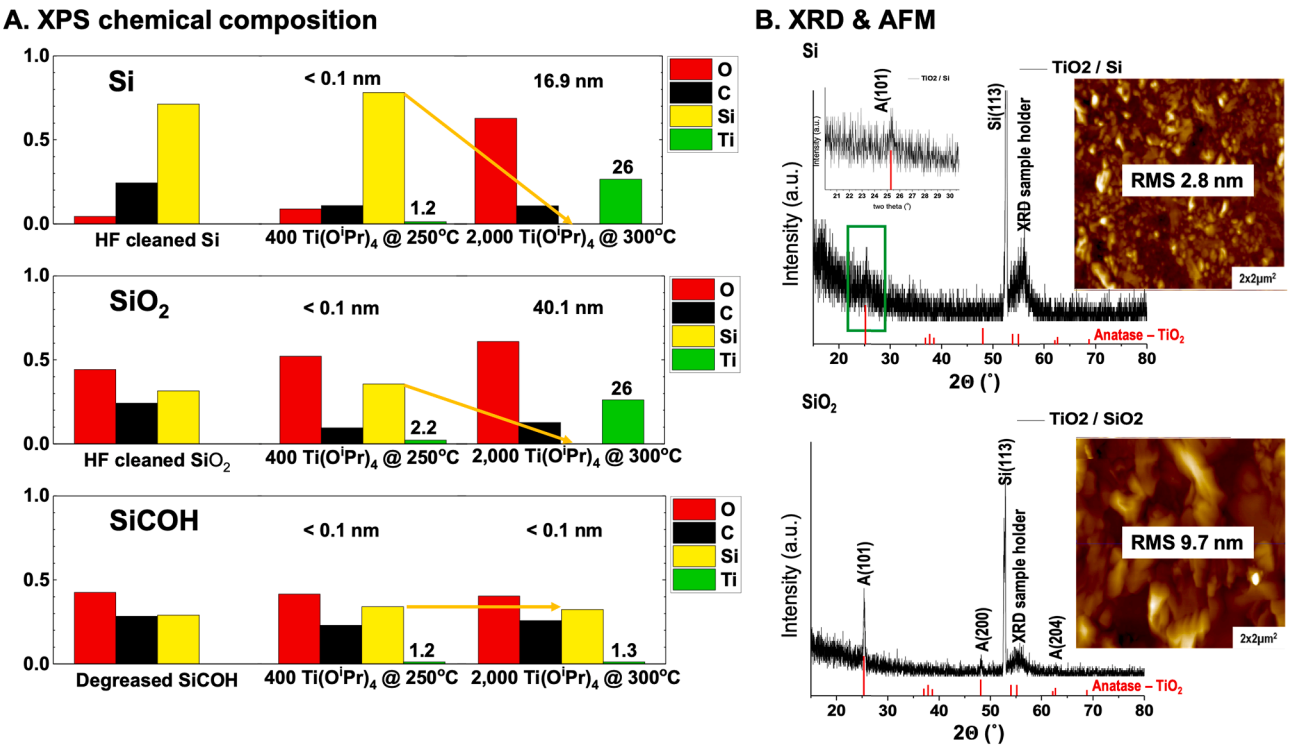

Fig. 2. Analysis of Pulsed CVD TiO_2 Films at 300 °C. (A) XPS chemical composition of HF cleaned Si, HF cleaned SiO_2 and degreased SiCOH after doses of Ti$(O^iPr)_4$ at 250 °C (negligible amount of nucleation) and 300 °C, and (B) XRD and AFM images of TiO_2 film on Si and SiO_2.

of the HfO_2/TiO_2 nanolaminate structure and sublayer thickness influence on crystallization. Finally, HfO_2/TiO_2 nanolaminate selective pulsed CVD was tested on Cu/SiCOH nanoscale patterned sample to evaluate the potential for nanoscale patterning applications. While the selectivity of the HfO_2/TiO_2 nanolaminate pulsed CVD deposition is similar to TiO_2/Al_2O_3 nanolaminate pulsed CVD also reported by the authors[27], HfO_2/TiO_2 are expected to be easier to etch than TiO_2/Al_2O_3 nanolaminates and therefore advantageous.[32–35] In addition, by employing chemically similar precursors for the Ti and Hf, it is possible to determine how the selectivity of each precursor contributes to the overall selectivity of the nanolaminate deposition.

2. Experimental

In this study, the selective pulsed CVD process for HfO_2/TiO_2 nanolaminate film was tested on three different substrates: Si, SiO_2, and SiCOH. Each substrate was diced into ~ 2 × ~ 12 mm rectangles so that three samples could be loaded on one sample holder. Samples were wet-cleaned before loading into the UHV chamber. The three samples were sequentially degreased with acetone, methanol, and deionized water for 15 s. To remove the surface native oxide, degreased Si and SiO_2 samples were immersed in a 0.5% diluted hydrofluoric acid solution for 30 s. After the wet cleaning, three samples were blown with an N_2 air gun to remove residual solution on the substrate surface. The samples were loaded to the UHV chamber on a single sample holder to go through the same dosing process to check the inherent selectivity. In addition to the selectivity test, HfO_2/TiO_2 nanolaminate pulsed CVD process was performed on a Cu/SiCOH nanoscale patterned sample. Cu/SiCOH patterned sample was wet-cleaned with the degreasing process explained above. Since the SiCOH region of the patterned sample was damaged from the initial fabrication process and, therefore, not fully covered with -OC_xH_y or -C_xH_y bonds, an additional passivation process was done with a proprietary passivation process from Applied Materials. After the passivation, the Cu/SiCOH patterned sample was loaded to the UHV chamber, together with a blanket SiCOH sample to check selective deposition on the Cu region only.

Fig. 1 shows a chamber schematic. A load lock chamber was employed to load and retrieve samples. The load lock chamber was pumped by a turbopump (Pfeiffer TPU 060) and a mechanical backing pump (Edwards RV3). The deposition chamber is also pumped by a turbopump (Pfeiffer TPU 060) and a mechanical backing pump (Edwards RV3). The base pressure of the deposition chamber was about 10^{-7} Torr. The deposition chamber contained a manipulator with a Cu sample mounting holder. A cartridge heater, inserted inside the Cu platform, heated the samples. Dosing lines for the precursors and nitrogen purge gas were connected to the deposition chamber. The precursor pulse pressure was controlled through a pneumatic valve, and no push gas was used. The deposition chamber wall and dosing lines were kept at 150 °C. The connected chamber was employed for *in-vacuo* X-ray photoelectron spectroscopy (XPS). The chamber was maintained at UHV pressure (low 10^{-9} Torr) and pumped by an ion pump (Agilent Varian VacIon 300 StarCell). An *in-vacuo* transfer was performed between deposition and XPS analysis so that the samples were not exposed to the ambient air prior to XPS, which could cause unwanted contamination or oxidation.

N_2 gas was continuously purged during the pulsed CVD process to remove the residual precursors inside the dosing chamber. Precursor dosing was monitored by the pressure spikes inside the deposition chamber and controlled by the precursor bottle temperature and the pneumatic valve open time. The Ti$(O^iPr)_4$ bottle was kept at room temperature (~21 °C), and the Hf$(O^tBu)_4$ bottle was heated up to 40 °C. The dosing time for each precursor was set to 50 ms and 200 ms for Ti$(O^iPr)_4$ and Hf$(O^tBu)_4$, respectively.

To check the crystallization from single oxide deposition and the selectivity of pulsed CVD for single oxide film deposition, single precursor pulsed CVD of TiO_2 and HfO_2 with Ti$(O^iPr)_4$ and Hf$(O^tBu)_4$, respectively, were studied. For TiO_2 pulsed CVD, multiple pulses of Ti$(O^iPr)_4$ were dosed between 250 °C and 300 °C sample temperature. Multiple pulses were employed instead of long single pulses due to the turbomolecular pumping of the ALD chamber. Between each Ti$(O^iPr)_4$

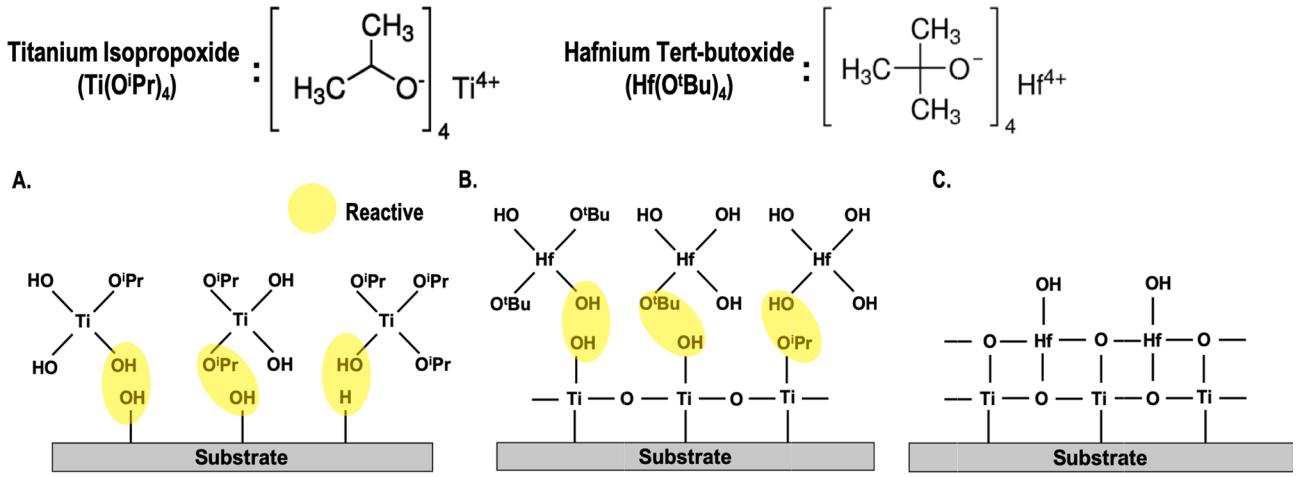

Fig. 3. The chemical structures of $Ti(O^iPr)_4$ and $Hf(O^tBu)_4$ and the proposed reaction mechanism for the HfO_2/TiO_2 nanolaminate film. (A). Thermal decomposition of $Ti(O^iPr)_4$ forms hydroxyl ligand which readily react with hydroxyl (SiO_2) or hydrogen (Si) bonds on the substrate surface and nucleate pulsed CVD. (B). Sequentially dosed $Hf(O^tBu)_4$) also thermally decomposes and reacts on TiO_2 on the surface. (C). HfO_2/TiO_2 nanolaminate film deposited.

pulse, 5 s of purging time was employed to remove residual and physisorbed precursor. For HfO_2 pulsed CVD, multiple pulses of $Hf(O^tBu)_4$ were dosed at 300 °C with 60 s interval between pulses. For HfO_2/TiO_2 nanolaminate CVD, the sample temperature was kept at 300 °C. Multiple pulses of $Ti(O^iPr)_4$ and $Hf(O^tBu)_4$ were dosed in each cycle. The purge time between $Ti(O^iPr)_4$ pulses and $Hf(O^tBu)_4$ pulses was 5 and 60 s, respectively. The number of pulses per cycle was controlled between 20 and 100 pulses for $Ti(O^iPr)_4$ and 1 and 5 for $Hf(O^tBu)_4$ to tune the Hf:Ti ratio of the nanolaminate film. The $Hf(O^tBu)_4$ is more reactive than the $Ti(O^iPr)_4$ precursor; therefore, less $Hf(O^tBu)_4$ pulse was dosed per cycle. The purge time between $Ti(O^iPr)_4$ and $Hf(O^tBu)_4$ was 60 s to remove all the residue from previous pulses.

After the pulsed CVD process, the samples were transferred to the XPS chamber, and *in-vacuo* XPS analysis was performed. A monochromatic Al Kα source (1486.7 eV) and a hemispherical analyzer (XM 1000 MkII/SPHERA, Omicron Nanotechnology) were employed. The anode voltage and the filament emission current were set to 10 kV and 25 mA, respectively, with hemisphere analyzer pass energy of 50 eV. The XPS detector was aligned to 60° from the sample surface normal. The peak shape analysis was performed with CASA XPS v.2.3 program and utilized Shirley background subtraction. The chemical compositions were normalized to the sum of all elements. After the whole in-situ CVD and XPS process, the morphology of the film was analyzed with ex-situ atomic force microscopy (AFM) (Agilent 5500) in tapping mode. For film thickness measurement, the oxide film thickness was derived based on Si substrate XPS signal attenuation when Si substrate signal was still detectable (film thickness less than 6 nm).[2,36] When Si signal was not detected (film thickness more than 6 nm), the film thickness was later measured by ex-situ ellipsometry (J. A. Woollam M−2000D). For crystallization study and nanoscale selectivity test, grazing incidence X-ray diffraction (GIXRD) (Rigaku SmartLab, Cu anode operating at 2 kW, parallel beam configuration, fixed 1.005° incidence angle) and transmission electron microscopy (TEM) were performed.

3. Results and discussion

3.1. Selectivity and crystallization study on single oxide film

To check both the selectivity and the crystallization in single oxide films, single oxide pulsed CVD was tested. Since metal alkoxide precursors [$Ti(O^iPr)_4$ and $Hf(O^tBu)_4$] contain oxygen in their ligands, Ti $(O^iPr)_4$ and $Hf(O^tBu)_4$ can form oxide film by unimolecular thermal decomposition.[2,36]

Fig. 2 shows the XPS chemical composition on Si, SiO_2, and SiCOH during the TiO_2 pulsed CVD process, which the authors previously reported.[2] (X-ray photoelectron spectra of each element-specific binding region are shown in Supporting Information Figure S1.) At 250 °C, 400 pulses of $Ti(O^iPr)_4$ barely decomposed and induced only a negligible CVD reaction (less than one monolayer) on any substrates. As the sample temperature increased to 300 °C, $Ti(O^iPr)_4$ induced a pulsed CVD reaction through thermal decomposition. After 2,000 pulses at 300 °C, Si peaks (Si 2p) were fully attenuated from Si and SiO_2. The thickness of TiO_2 on Si and SiO_2 were 16.9 nm and 40.1 nm, respectively. On SiCOH, however, 1.3% of Ti was detected, which corresponds to less than a monolayer of TiO_2. This selective deposition was due to the inherent reactivity difference for precursor mediated chemisorption of $Ti(O^iPr)_4$ on each surface.

Ex-situ AFM was performed to check the film morphology. As shown in Fig. 2, the thick TiO_2 films on Si and SiO_2 had 2.8 nm and 9.7 nm RMS roughness. GIXRD analysis proved that the rough TiO_2 films on Si and SiO_2 were due to crystallization. The 16.9 nm TiO_2 film on Si exhibited a small anatase (1 0 1) peak. For the 40.1 nm TiO_2 film on SiO_2, crystallization became more significant. GIXRD for the 40.1 nm TiO_2 film on SiO_2 showed anatase (1 0 1), (2 0 0), and (2 0 4) peaks, and the intensity of the (1 0 1) peak was higher than the intensity of the peak from Si substrate. These results are consistent with crystallization increasing with TiO_2 film thickness. This crystallization issue, which caused nm scale film roughness, can be a problem for its application to nanoscale patterning.

HfO_2 CVD with $Hf(O^tBu)_4$ was tested at 300 °C. The XPS chemical composition and the AFM images for HfO_2 films on the substrates are shown in Supporting Information Figure S2. (X-ray photoelectron spectra of each element-specific binding region are shown in Supporting Information Figure S3.) After 100 $Hf(O^tBu)_4$ pulses, 1.80 nm and 5 nm of HfO_2 film were deposited on Si and SiO_2 at 300 °C, while SiCOH had less than a monolayer (0.13 nm) of HfO_2. Compared to TiO_2 CVD with Ti $(O^iPr)_4$ above, HfO_2 CVD showed lower selectivity. The lower selectivity could be due to the difference in surface reactivity of isopropoxide (O^iPr) ligand and butoxide (O^tBu) ligand precursor. HfO_2 films on Si and SiO_2 showed RMS roughness of 0.49 nm and 0.66 nm, respectively, with 2–4 nm tall particles. The particles could be due to the onset of crystallization as thicker HfO_2 films on SiO_2 showed higher roughness than the thinner HfO_2 films on Si. XRD was not performed because the films were sub 5 nm, but previous research proved that the HfO_2 process induces crystallization at 300 °C as the film thickness increases.[19]

The single precursor CVD of TiO_2 with $Ti(O^iPr)_4$ and HfO_2 with Hf $(O^tBu)_4$ proved that selective oxide deposition could be achieved with a metal alkoxide precursor. The selectivity was determined by the

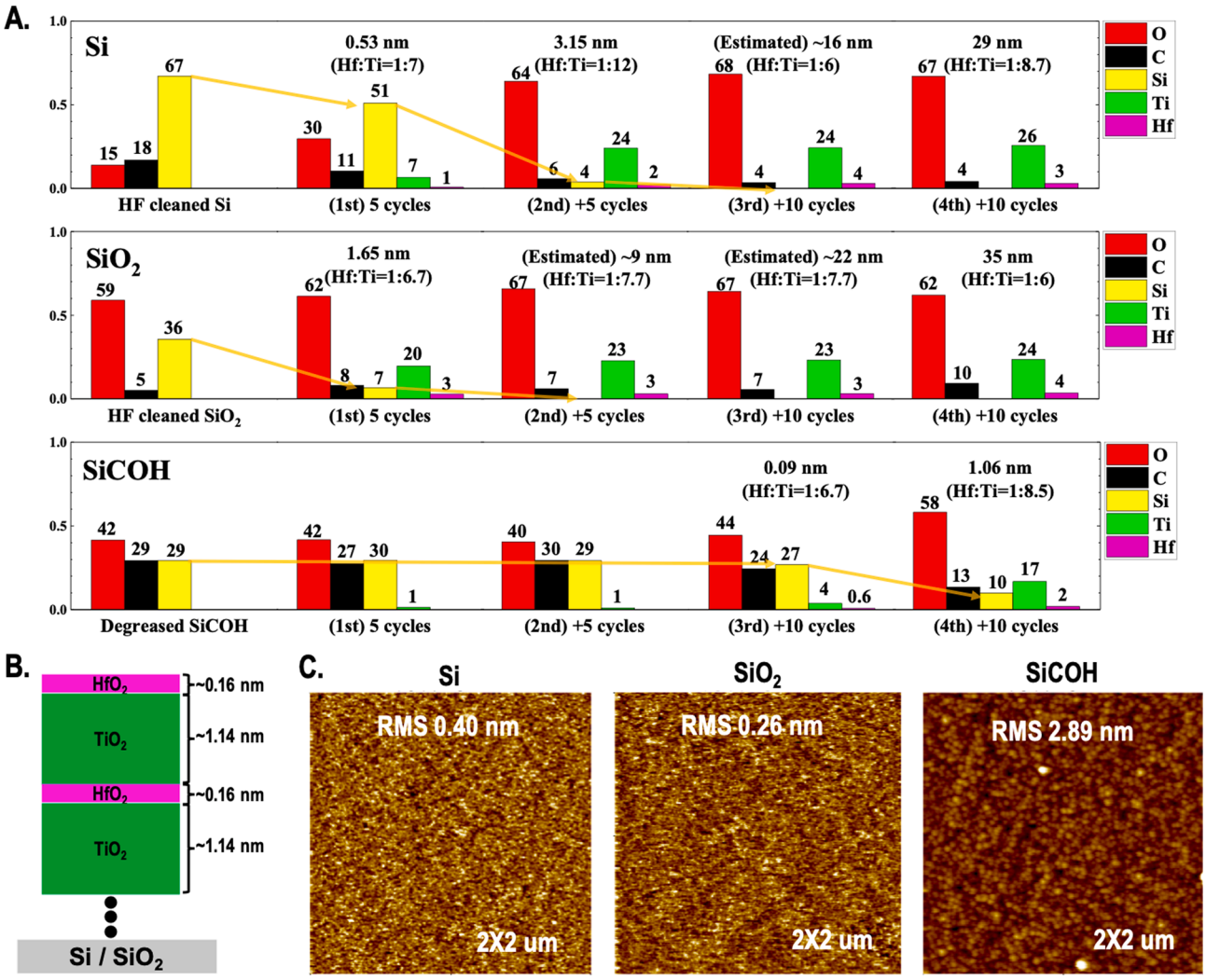

Fig. 4. Analysis of 300 °C Pulsed CVD of Highly Ti-rich HfO_2/TiO_2 Films. (A). XPS chemical composition, (B) estimated nanolaminate structure, and (C) AFM of Si, SiO_2, and SiCOH after total 30 cycles of the highly Ti-rich HfO_2/TiO_2 nanolaminate CVD process.

precursor for each process. However, as shown with the TiO_2 films in this study and by others[2,19], oxide films have increased crystallinity and corresponding roughness with increasing film thickness. To solve this crystallization issue, a nanolaminate structure with HfO_2 and TiO_2 was studied.

3.2. *Selectivity study of the HfO_2/TiO_2 nanolaminate film*

A proposed reaction mechanism of the HfO_2/TiO_2 nanolaminate film is described in Fig. 3, consistent with other published mechanisms. [2,36] In the 1st step (Fig. 3. A), $Ti(O^iPr)_4$ is dosed on the substrate at 300 °C. Due to the high temperature, $Ti(O^iPr)_4$ decomposes and forms hydroxyl ligands. The hydroxyl is more reactive than the isopropoxide so that the decomposed precursor starts to react with hydrogen bonds on Si and hydroxyl bonds on SiO_2 and forms a TiO_2 film. After the $Ti(O^iPr)_4$ pulse, $Hf(O^tBu)_4$ is dosed (Fig. 3. B). With the same mechanism, Hf $(O^tBu)_4$ decomposes and reacts on the TiO_2 and forms the nanolaminate structure (Fig. 3. C). Since SiCOH has $-OC_xH_y$ or $-C_xH_y$ bond, which is not reactive, it is hypothesized that deposition will not occur on the ideal SiCOH surface, inducing selective deposition. However, the precursor starts to react on minor reactive defect sites or physisorbs on SiCOH, inducing loss of selectivity.

The HfO_2/TiO_2 nanolaminate film CVD process was performed as described in the experimental section. Three different Hf:Ti ratio nanolaminate films were fabricated by controlling the number of Ti $(O^iPr)_4$ and $Hf(O^tBu)_4$ pulses per cycle. From their Hf:Ti ratios, the samples were denoted as Hf-rich (Hf:Ti ratio: ~4:1), Ti-rich (Hf:Ti ratio: 1:~2.5), and highly Ti-rich (Hf:Ti ratio: 1:~7) nanolaminate films.

Fig. 4 shows XPS chemical composition, estimated nanolaminate structure, and AFM images of the highly Ti-rich HfO_2/TiO_2 samples (X-ray photoelectron spectra of each element-specific binding region are shown in Supporting Information Figure S4.). For the highly Ti-rich nanolaminates, 100 pulses of $Ti(O^iPr)_4$ and 1 pulse of $Hf(O^tBu)_4$ were dosed per cycle. During the first few cycles, the samples were in the nucleation period; growth was slow, consistent with nuclei formation on the substrate surface. However, after additional deposition, the film had fast and constant deposition per cycle. For example, for the Si sample in Fig. 4, during the 1st 10 cycles, Si had 3.15 nm deposition, which means the average growth rate during 1st 10 cycles was around 0.32 nm/cycle. However, after an additional 20 cycles, the overall film thickness on Si was 29 nm, corresponding to a growth of 1.3 nm/cycle during the last 20 cycles. With this constant growth rate after the nucleation period and Hf:Ti ratio, the nanolaminate structure was estimated, as shown in Fig. 4. B. The SiO_2 substrate also had a nucleation period with slow growth. However, consistent with the hydroxyls on the SiO_2 surface being more reactive than hydrogens on the Si surface, SiO_2 exhibited faster nucleation than Si.

The selective deposition of highly Ti-rich HfO_2/TiO_2 nanolaminate

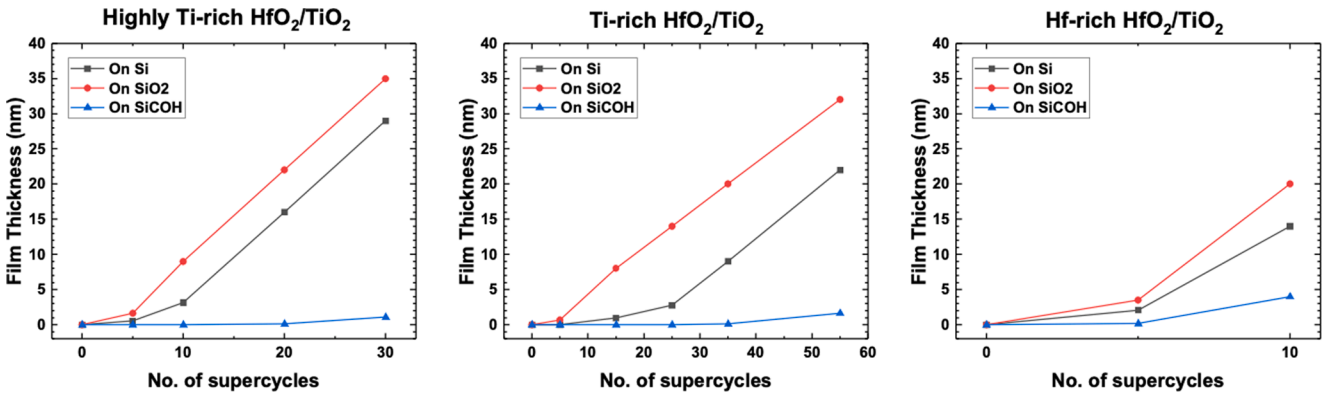

Fig. 5. Film thickness on Si, SiO_2, and SiCOH for three different Hf:Ti ratio HfO_2/TiO_2 nanolaminates by pulsed CVD. Maximum y-axis (film thickness) values are set to 40 nm for all three graphs to compare thickness between the different processes.

can be observed in Fig. 4 A. After the 1st 10 cycles, 3.15 nm and 9 nm of films were deposited on Si and SiO_2, respectively, while only a 1% Ti peak and no Hf peak were detected from the SiCOH surface. After 10 more cycles, around ~ 16 nm (estimation from the growth rate after nucleation period) and ~ 22 nm of the nanolaminate films were deposited on Si and SiO_2, respectively, while the SiCOH had less than a monolayer (0.09 nm). After the last 10 more cycles, the thicknesses on Si, SiO_2, and SiCOH were 29 nm, 35 nm, and 1.06 nm, respectively. Therefore, it was observed that SiCOH had a significant nucleation delay for highly Ti-rich HfO_2/TiO_2, but the selectivity relative to Si and SiO_2 of the pulsed CVD process decreased as the number of cycles increased.

Fig. 4 C shows AFM images of highly Ti-rich HfO_2/TiO_2 nanolaminate films on Si, SiO_2, and SiCOH. The nanolaminate films on Si and SiO_2 were smooth films with the RMS roughness 0.40 nm and 0.26 nm, respectively, without any significant particles. Compared to the AFM images of pure TiO_2 and HfO_2 films shown in Fig. 2 and Figure S2, the nanolaminate films showed smoother films (for comparable thicknesses) without any particles. Further study of the film roughness of the nanolaminate will be covered in the next section. The RMS roughness on SiCOH was high (2.89 nm) because the film thickness on SiCOH (1.06 nm) was not sufficient to cover the whole surface.

XPS chemical compositions, AFM images, and estimated nanolaminate structure for Ti-rich and Hf-rich nanolaminates are shown in Supporting Information Figure S5 and S6, respectively (X-ray

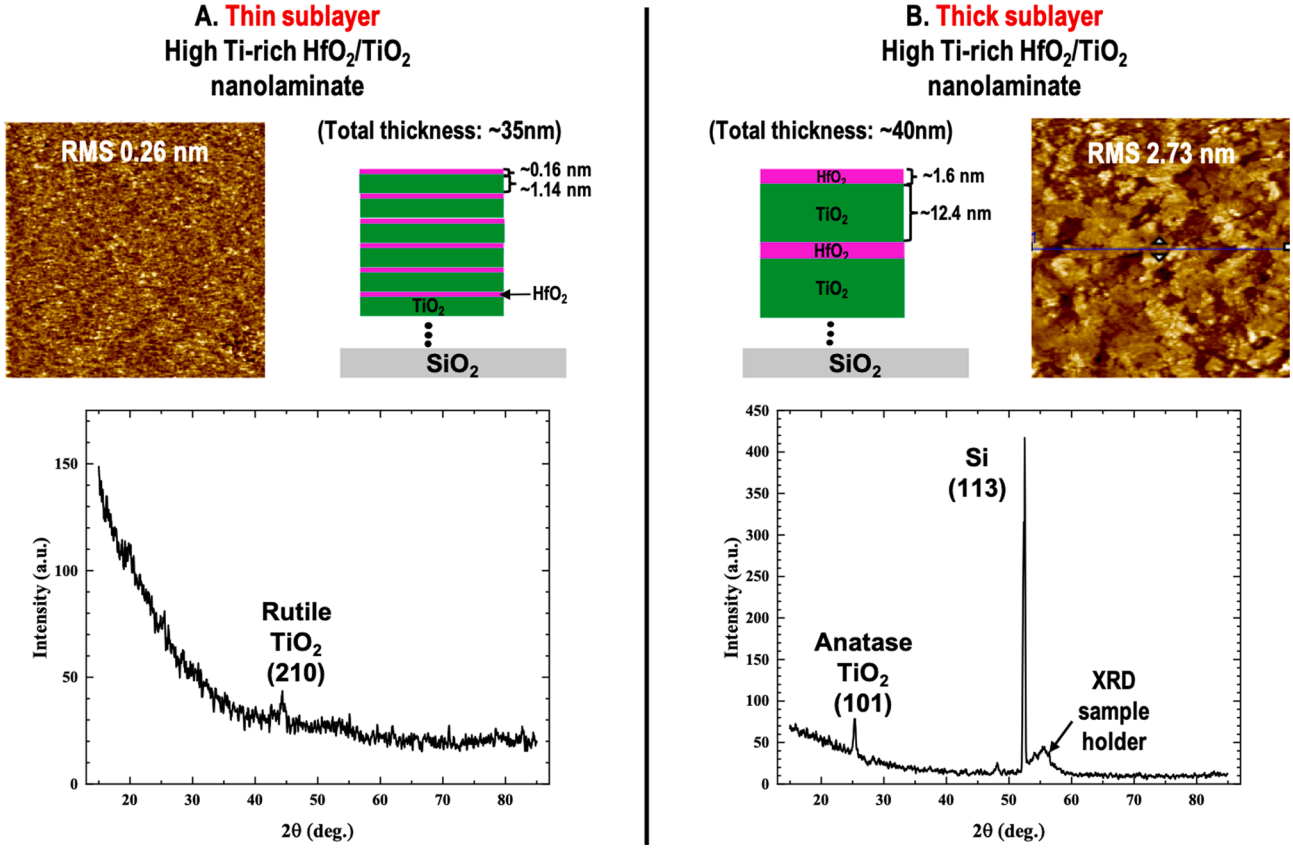

Fig. 6. AFM and XRD Study on the Effect of Sublayer Thickness on Crystallinity. (A) The thin sublayer nanolaminate film had a smooth surface with 0.26 nm RMS roughness. The film was almost amorphous, with only a tiny rutile TiO_2 (2 1 0) peak. (B) The thick sublayer (~10 × thicker sublayer) nanolaminate film with similar total thickness had a rough surface with 2.73 nm RMS roughness. The film showed clear anatase TiO_2 (1 0 1) peak, indicating that the nanolaminate structure could not prevent crystallization.

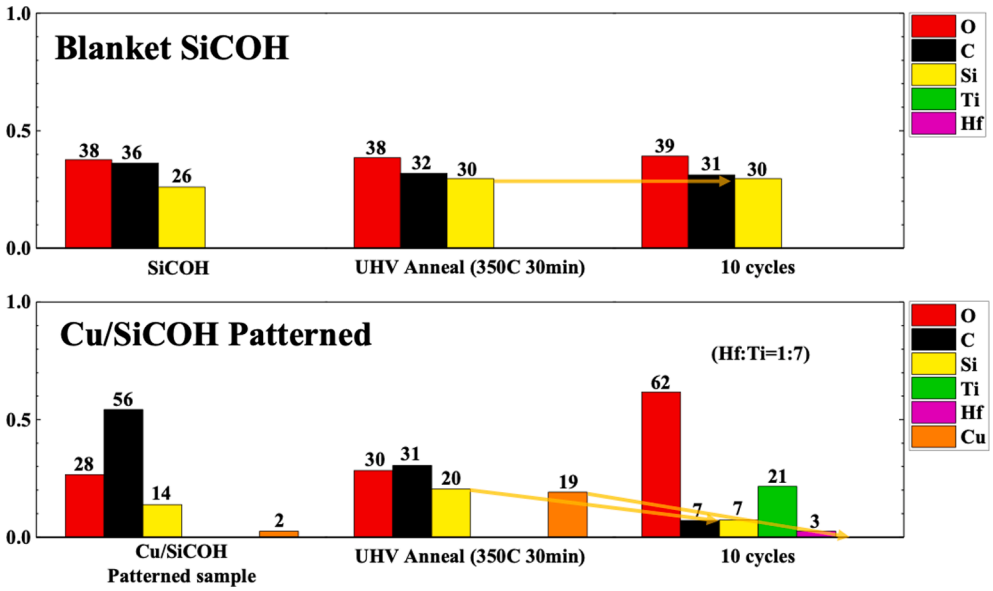

Fig. 7. XPS of Selective CVD of Highly Ti-rich HfO_2/TiO_2 Nanolaminates on a Nanoscale Patterned Sample. XPS chemical composition of blanket SiCOH and Cu/SiCOH patterned samples before and after 10 cycles of highly Ti-rich HfO_2/TiO_2 nanolaminate CVD process.

photoelectron spectra of each element-specific binding region are shown in Supporting Information Figure S7 for Ti-rich nanolaminate samples, and Supporting Information Figure S8 for Hf-rich nanolaminate samples.). All four nanolaminate films on Si and SiO_2 showed a smooth surface with around 0.4 nm RMS roughness. Hf-rich nanolaminate films had a few particles in the AFM images. The particle formation is consistent with the HfO_2 sublayer for the Hf-rich nanolaminate film being ~ 2.4 nm, which is thicker than any other sublayers and could initiate crystallization.

To analyze the selectivity of the HfO_2/TiO_2 nanolaminate film in more detail, the nanolaminate film thickness on each sample with three different compositions is shown in Fig. 5. As the Ti ratio increased, the nanolaminate films showed higher selectivity for thicker deposition, consistent with a greater nucleation delay on SiCOH for Ti-rich films. This tendency is affected by the selectivity of each single precursor CVD with $Ti(O^iPr)_4$ and $Hf(O^tBu)_4$. For example, TiO_2 CVD with $Ti(O^iPr)_4$ showed ~ 17 nm and ~ 40 nm selective deposition on Si and SiO_2, respectively. Conversely, HfO_2 CVD with $Hf(O^tBu)_4$ showed only ~ 2 nm and ~ 5 nm selective deposition on Si and SiO_2. In addition, the films on SiO_2 showed higher selectivity than the films on Si. It is consistent with the hydroxyl bonds on SiO_2 having higher reactivity than hydrogen bonds on Si, and, therefore, more rapid nucleation occurs on SiO_2.

3.3. Crystallization study of the HfO_2/TiO_2 nanolaminate film

AFM indicated that the nanolaminate films were smooth with less than 0.5 nm RMS roughness which was a clear difference in film roughness compared to the single oxide films with similar thickness. A detailed study on the effect of the nanolaminate structure on film crystallization was performed. To check both the effects of nanolaminate structure and sublayer thickness on film crystallization, XRD analysis was performed on two different samples. The 1st sample (Fig. 6 A) is highly Ti-rich HfO_2/TiO_2 nanolaminate film with thin sublayers on SiO_2, the same sample as shown in Fig. 4. The estimated sublayer thickness for this sample was around 1.14 nm and 0.16 nm for TiO_2 and HfO_2, respectively. The total thickness of the nanolaminate film was 35 nm. The 2nd sample had similar a Hf:Ti ratio (1:~7) and total thickness (~40 nm) but thicker sublayers (Fig. 6 B). The sublayer thicknesses were 12.4 nm and 1.6 nm for TiO_2 and HfO_2, respectively, around 10x thicker than those of the thin sublayer sample.

The AFM images of the two samples showed a significant difference. The RMS roughness of the thin sublayer sample was 0.26 nm which was a similar range with other nanolaminate films. However, the RMS roughness of the thick sublayer sample was 2.73 nm, which is closer to that of the thick TiO_2 film shown in Fig. 2. From the XRD pattern, the thin sublayer sample showed a tiny rutile TiO_2 (2 1 0) peak; however, no prominent peaks were detected consistent with an almost amorphous structure. However, the thick sublayer sample showed a clear anatase TiO_2 (1 0 1) peak, proving that the film had crystallization consistent with its rough surface. Conversely, the HfO_2 crystallization peak was not detected even from the thick sublayer sample; the HfO_2 sublayer thickness was around 1.6 nm, which could be lower than its critical thickness to induce crystallization. It was shown from previous experiments that HfO_2 and TiO_2 single oxide films could induce crystallization as film thickness increases.[2,19] However, in the nanolaminate structure of these oxides, the crystallization could be suppressed as long as each HfO_2 and TiO_2 sublayer thickness is below their critical thicknesses to induce crystallization. It is noted that G. E. Testoni et al. documented similar limitations on sublayer thickness, but using at least one layer which is always amorphous, Al_2O_3.[20] In addition, previous research on HfO_2/TiO_2 structures also did not report on the limits on sublayer thickness for film crystallization.[24–26]

3.4. Selectivity in nm scale region for HfO_2/TiO_2 nanolaminate film

To apply the HfO_2/TiO_2 nanolaminate CVD process to nanoscale patterning, the process was performed on the passivated Cu/SiCOH nanoscale patterned sample. The passivation on the Cu region desorbed during 350C UHV anneal (30 min) before the CVD process. Therefore, the passivation selectively passivated the damaged SiCOH. A passivated blanket SiCOH sample was loaded with the patterned sample to check any deposition on the SiCOH surface.

In Fig. 7. shows the XPS chemical composition of the passivated blanket SiCOH and Cu/SiCOH patterned sample before and after 10 cycles of the highly Ti-rich HfO_2/TiO_2 nanolaminate pulsed CVD process (X-ray photoelectron spectra of each element-specific binding region are shown in Supporting Information Figure S9.). Before the pulsed CVD process, samples were annealed in UHV (low 10^{-9} Torr region) at 350 °C for 30 min to remove the surface contaminants. After UHV anneal, it was seen that carbon fraction significantly decreased on the patterned sample (56% → 31%). This was consistent with both carbon contaminants on the sample from ambient air and carbon from the passivant on

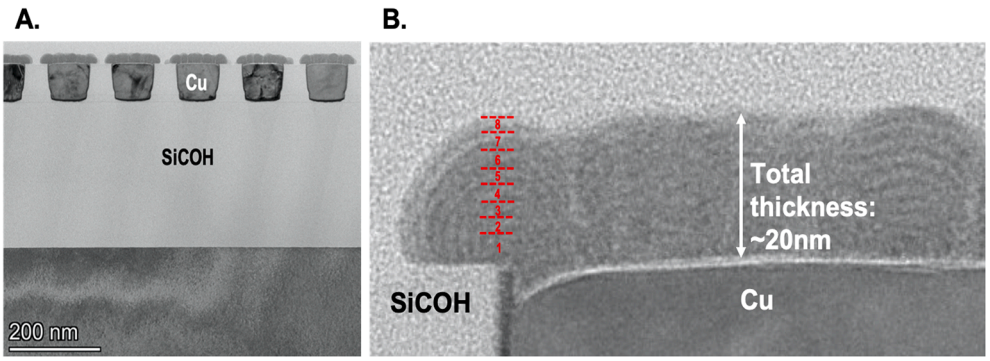

Fig. 8. TEM Analysis of Selective CVD of a Highly Ti-rich HfO_2/TiO_2 nanolaminate on a Nanoscale Patterned Sample (A) TEM image of Cu/SiCOH patterned sample after 10 cycles of highly Ti-rich HfO_2/TiO_2 nanolaminate CVD. (B) Magnified view of a nanolaminate film on Cu inlay. As can be seen from the TEM images, the nanolaminate film was deposited only on Cu. From the magnified view (B), around 8 cycles of grey/black pattern were observed from the film, consistent with the nanolaminate structure.

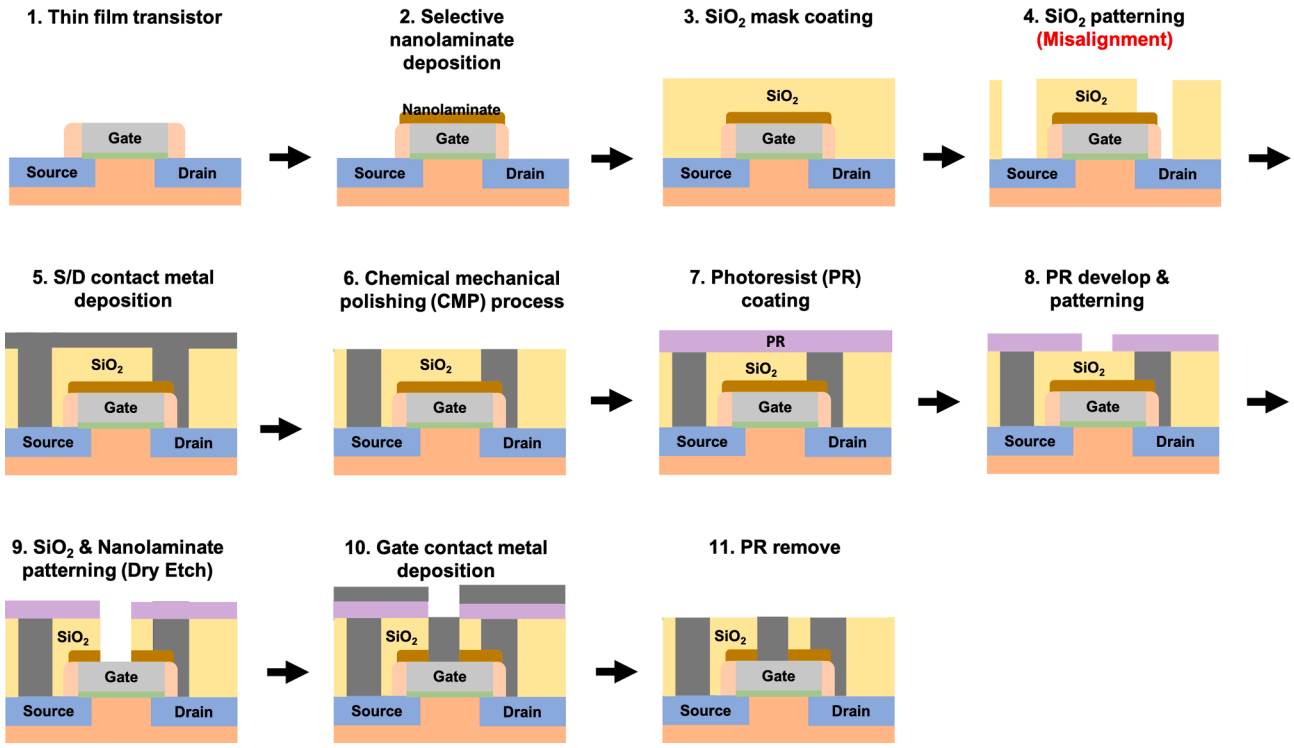

Fig. 9. Application of selective HfO_2/TiO_2 nanolaminate film deposition on gate electrodes By selectively depositing HfO_2/TiO_2 nanolaminate film on the gate electrode, it can protect the gate from sequential etch processes and prevent short circuits with source/drain contact metals, which can be caused by misalignment. The HfO_2/TiO_2 nanolaminate film is patterned afterward for the gate contact deposition.

Cu being desorbed. After 10 cycles of highly Ti-rich HfO_2/TiO_2 nanolaminate CVD, the Cu peak was fully attenuated, consistent with deposition on the Cu surface. Hf:Ti ratio was 1:7, which is close to previous samples on Si and SiO_2. The Si percentage from the SiCOH surface of the patterned sample also decreased from 20 % to 7 %, while the blanket SiCOH was still clean. The reason for the Si percentage decrease from the patterned sample became clear from the TEM image (Fig. 8).

In Fig. 8. shows the cross-sectional TEM image of the patterned sample from Fig. 7. after the nanolaminate deposition. The patterned sample was composed of SiCOH and Cu surface, and the width of each surface was 90 nm for Cu and 50 nm for SiCOH. From the TEM images, around 20 nm of HfO_2/TiO_2 nanolaminate film was deposited on the Cu surface. However, the nanolaminate film had isotropic growth, inducing a lateral growth over the SiCOH region consistent with the Si % decrease in the XPS data, as shown in Fig. 7. In the magnified view of the TEM image (Fig. 8 B), grey and black patterns were observed from the nanolaminate film. This pattern is consistent with the nanolaminate structure of HfO_2 and TiO_2 sublayers. The nanolaminate pattern had low contrast because each sublayer was ~ 1 nm. Around 8black/grey patterns were observed from the film, similar to the total number of cycles (10 cycles); this is consistent with the first two cycles forming a mixed oxide during the slow growth nucleation period. In conclusion, it is proven from the TEM study that the HfO_2/TiO_2 nanolaminate CVD process can have selective deposition in the nm scale region.

As the HfO_2/TiO_2 nanolaminate film showed selective deposition in the nm scale region, the above application in Fig. 9 was proposed. The nanolaminate oxide film can be selectively deposited on the gate electrode before the source/drain contact metal connection is made. The nanolaminate layer can protect the gate electrode from sequential etching processes. In addition, as the transistor size decreases to the nm scale, there is more chance that patterning misalignment can induce electrical shorts between the source/drain contacts and the gate electrode. The nanolaminate oxide can prevent the electrical shorts even if the misalignment occurs. After the source/drain contact metal connection, the nanolaminate film would be patterned for a gate contact metal connection. TiO_2/Al_2O_3 nanolaminate, previously reported by the authors[27], can be used in the same application. However, HfO_2/TiO_2 nanolaminate has an advantage in etching. Although, HfO_2, TiO_2, and

Al_2O_3 can be dry-etched with the CF_4 + Ar plasma process, the HfO_2 etch rate is higher and closer to the TiO_2 etch rate than the Al_2O_3 etch rate. [32–35] Therefore, the HfO_2/TiO_2 nanolaminate film has a faster etch rate and may have higher etch selectivity to photoresist compared to the TiO_2/Al_2O_3 nanolaminate film. Due to this advantage in the etching process, HfO_2/TiO_2 nanolaminate is expected to be more favorable for certain applications.

4. Conclusion

Inherent selective deposition of amorphous HfO_2/TiO_2 nanolaminate film was studied. Metal alkoxide precursors, e.g., $Hf(O^tBu)_4$ and $Ti(O^iPr)_4$, can form oxide film without any oxygen co-reactant such as water. This enables investigation of halogen-free selective deposition on nanoscale patterned with a water-sensitive insulator such as SiCOH and halogen-sensitive metals such as Cu. Two precursors of a similar composition containing oxygen were studied, enabling investigation of the mechanisms of selectivity and crystallization control in a pulsed CVD process for selective nanolaminate formation. Due to the reactivity difference of precursors on Si, SiO_2, and SiCOH, the film was selectively deposited on Si and SiO_2 before nucleation occurred on SiCOH. The selectivity of the nanolaminate film was controlled by the ratio of each precursor. Since $Ti(O^iPr)_4$ showed higher selectivity than $Hf(O^tBu)_4$, up to ~ 20 nm of selective deposition on Si and SiO_2 was achieved with highly Ti-rich (Hf:Ti ratio: 1:~7) nanolaminate film before significant nucleation occurred on SiCOH. The film was almost amorphous with less than 0.4 nm RMS roughness. However, if the sublayers were thicker than their critical thickness to induce crystallization, even the nanolaminate structure could not prevent crystallization. The nanolaminate CVD process showed around 20 nm of selective deposition on the Cu region from the Cu/SiCOH nanoscale patterned sample. Compared to TiO_2/Al_2O_3 nanolaminate pulsed CVD[27], the HfO_2/TiO_2 nanolaminate film in this study is more suitable for subsequent etching.[32–35] Therefore, the selective amorphous HfO_2/TiO_2 nanolaminate CVD process can be suitable for the nanoscale hard mask in the patterning process for nanometer-scale MOSFET fabrication.

CRediT authorship contribution statement

Yunil Cho: Conceptualization, Methodology, Formal analysis, Investigation, Writing – original draft. **James Huang:** Methodology, Formal analysis, Investigation. **Christopher F. Ahles:** Formal analysis, Investigation. **Zichen Zhang:** Formal analysis. **Keith Wong:** Writing – review & editing, Resources. **Srinivas Nemani:** . **Ellie Yieh:** Supervision. **Andrew C. Kummel:** Writing – review & editing, Supervision.

Declaration of Competing Interest

The authors declare that they have no known competing financial interests or personal relationships that could have appeared to influence the work reported in this paper.

Acknowledgements

Funding support from Applied Materials is gratefully acknowledged. The electrical measurements were facilitated by the San Diego Nanotechnology Infrastructure (SDNI) which is supported by the National Science Foundation (NSF) to Nano3 (Grant ECCS-1542148).

Appendix A. Supplementary material

Supplementary data to this article can be found online at https://doi.org/10.1016/j.apsusc.2022.154010.

References

[1] www.beneq.com/en/technology.
[2] Y. Cho, C.F. Ahles, J.Y. Choi, J. Huang, A. Jan, K. Wong, S. Nemani, E. Yieh, A. C. Kummel, Inherently Selective Water-Free Deposition of Titanium Dioxide on the Nanoscale: Implications for Nanoscale Patterning, ACS Appl. Nano Mater. 5 (1) (2022) 476–485.
[3] H. Li, D.B. Farmer, R.G. Gordon, Y. Lin, J. Vlassak, Vapor Deposition of Ruthenium from an Amidinate Precursor, Journal of The Electrochemical Society 154 (12) (2007) D642–D647.
[4] A.J.M. Mackus, A.A. Bol, W.M.M. Kessels, The use of atomic layer deposition in advanced nanopatterning, Nanoscale 6 (19) (2014) 10941–10960.
[5] S. Atanasov, B. Kalanyan, G.N. Parsons, Inherent substrate-dependent growth initiation and selective-area atomic layer deposition of TiO2 using "water-free" metal-halide/metal alkoxide reactants, Journal of Vacuum Science and Technology A 34 (2016).
[6] M. Yang, A.A.I. Aarnink, J. Schmitz, A.Y. Kovalgin, Inherently area-selective hot-wire assisted atomic layer deposition of tungsten films, Thin Solid Films 649 (2018) 17–23.
[7] J.Y. Choi, C.F. Ahles, R. Hung, N. Kim, A.C. Kummel, Selective atomic layer deposition of $MoSi_x$ on Si (001) in preference to silicon nitride and silicon oxide, Applied Surface Science 462 (2018) 1008–1016.
[8] P.C. Lemaire, M. King, G.N. Parsons, Understanding inherent substrate selectivity during atomic layer deposition: Effect of surface preparation, hydroxyl density, and metal oxide composition on nucleation mechanisms during tungsten ALD, J. Chem. Phys. 146 (2017), 052811.
[9] T. Suh, Y. Yang, P. Zhao, K.U. Lao, H.-Y. Ko, J. Wong, R.A. DiStasio, J.R. Engstrom, Competitive Adsorption as a Route to Area-Selective Deposition, ACS Appl. Mater. Interfaces 12 (8) (2020) 9989–9999.
[10] D. Bobb-Semple, K.L. Nardi, N. Draeger, D.M. Hausmann, S.F. Bent, Area-Selective Atomic Layer Deposition Assisted by Self-Assembled Monolayers: A Comparison of Cu Co, W, and Ru, Chem. Mater. 31 (2019) 1635–1645.
[11] F.S.M. Hashemi, S.F. Bent, Sequential Regeneration of Self-Assembled Monolayers for Highly Selective Atomic Layer Deposition, Advanced Materials Interfaces 3 (2016) 1600464.
[12] F.S.M. Hashemi, C. Prasittichai, S.F. Bent, A new resist for area selective atomic and molecular layer deposition on metal-dielectric patterns, The Journal of Physical Chemistry C 118 (2014) 10957.
[13] F.S.M. Hashemi, B.R. Birchansky, S.F. Bent, Selective Deposition of Dielectrics: Limits and Advantages of Alkanethiol Blocking Agents on Metal−Dielectric Patterns, ACS Appl. Mater. Interfaces 8 (2016) 33264–33272.
[14] C. Prasittichai, K.L. Pickrahn, F.S. Minaye Hashemi, D.S. Bergsman, S.F. Bent, Improving Area-Selective Molecular Layer Deposition by Selective SAM Removal, ACS Appl. Mater. Interfaces 6 (20) (2014) 17831–17836.
[15] A. Mameli, B. Karasulu, M.A. Verheijen, B. Barcones, B. Macco, A.J.M. Mackus, W. M.M.E. Kessels, F. Roozeboom, Area-Selective Atomic Layer Deposition of ZnO by Area Activation Using Electron Beam-Induced Deposition, Chem. Mater. 31 (4) (2019) 1250–1257.
[16] A. Mameli, Y. Kuang, M. Aghaee, C.K. Ande, B. Karasulu, M. Creatore, A.J. M. Mackus, W.M.M. Kessels, F. Roozeboom, Area-Selective Atomic Layer Deposition of In_2O_3: H Using a u-Plasma Printer for Local Area Activation, Chem. Mater. 29 (2017) 921–925.
[17] E. Färm, S. Lindroos, M. Ritala, M. Leskelä, Microcontact Printed RuO_x Film as an Activation Layer for Selective-Area Atomic Layer Deposition of Ruthenium, Chem. Mater. 24 (2) (2012) 275–278.
[18] A.J.M. Mackus, J.J.L. Mulders, M.C.M. van de Sanden, W.M.M. Kessels, Local deposition of high-purity Pt nanostructures by combining electron beam induced deposition and atomic layer deposition, Journal of Applied Physics 107 (2010), 116102.
[19] R. Rammula, J. Aarik, H. Mandar, P. Ritslaid, V. Sammelselg, Atomic layer deposition of HfO2: Effect of structure development on growth rate, morphology and optical properties of thin films, Applied Surface Science 257 (2010) 1043–1052.
[20] G.E. Testoni, W. Chiappim, R.S. Pessoa, M.A. Fraga, W. Miyakawa, K.K. Sakane, N. K.A.M. Galvao, L. Vieira, H.S. Maciel, Influence of the Al_2O_3 partial-monolayer number on the crystallization mechanism of TiO_2 in ALD TiO_2/Al_2O_3 nanolaminates and its impact on the material properties, J. Phys. D: Appl. Phys. 49 (2016), 375301.
[21] J.W. Elam, Z.A. Sechrist, S.M. George, ZnO/ Al_2O_3 nanolaminates fabricated by atomic layer deposition: growth and surface roughness measurements, Thin Solid films 414 (1) (2002) 43–55.
[22] I. Iatsunskyi, E. Coy, R. Viter, G. Nowaczyk, M. Jancelewicz, I. Baleviciute, K. Załęski, S. Jurga, Study on Structural, Mechanical, and Optical properties of Al_2O_3-TiO_2 Nanolaminates Prepared by Atomic Layer Deposition, J. Phys. Chem. C 119 (35) (2015) 20591–20599.
[23] D.M. Hausmann, R.G. Gordon, Surface morphology and crystallinity control in the atomic layer deposition (ALD) of hafnium and zirconium oxide thin films, Journal of Crystal Growth 249 (1-2) (2003) 251–261.
[24] D.H. Triyoso, R.I. Hegde, S. Zollner, M.E. Ramon, S. Kalpat, R. Gregory, X.-D. Wang, J. Jiang, M. Raymond, R. Rai, D. Werho, D. Roan, W.B.E. Jr, P.J. Tobin, Impact of titanium addition on film characteristics of HfO_2 gate dielectrics deposited by atomic layer deposition, Journal of Applied Physics 98 (2005), 054104.
[25] D.H. Triyoso, R.I. Hegde, X.-D. Wang, M.W. Stoker, R. Rai, M.E. Ramon, W.B.E. Jr, P.J. Tobin, Characteristics of Mixed Oxides and Nanolaminates of Atomic Layer

Deposited HfO_2-TiO_2 gate Dielectrics, Journal of The Electrochemical Society 153 (9) (2006).
[26] B. Lee, A. Hande, T.J. Park, K.J. Chung, J. Ahn, M. Rousseau, D. Hong, H. Li, X. Liu, D. Shenai, J. Kim, ALD of $LaHfO_x$ nano-laminates for high-k gate dielectric applications, Microelectronic Engineering 88 (2011) 3385–3388.
[27] J. Huang, Y. Cho, Z. Zhang, A. Jan, K.T. Wong, S. Nemani, E. Yieh, A.C. Kummel, Selective Pulsed Chemical Vapor Deposition of Water-Free TiO_2/Al_2O_3 and HfO_2/Al_2O_3 Nanolaminates on Si and SiO2 in Preference to SiCOH, ACS Appl. Mater. Interfaces 14 (13) (2022) 15716–15727.
[28] V. McGahay, Porous Dielectrics in Microelectronic Wiring Applications, Materials 3 (2010) 536–562.
[29] A. Grill, Plasma enhanced chemical vapor deposited SiCOH dielectrics: from low-k to extreme low-k interconnect materials, Journal of Applied Physics 93 (2003) 1785.
[30] Edelstein, D. C.; Gates, S. M.; Grill, A.; Lane, M.; Miller, R. D.; Neunmayer, D. A.; Nguyen, S. V.; SiCOH dielectric material with improved toughness and improved Si-C bonding, semiconductor device containing the same, and method to make the same. US 2005/0194619 A1.
[31] Canaperi, D. F.; Nguyen, S. V.; Priyadarshini, D.; Shobha, H. K.; Advanced ultra low k SiCOH dielectrics prepared by built-in engineered pore size and bonding structured with cyclic organosilicon. US 9209017 B2.
[32] P.S. Kang, J.C. Woo, Y.H. Joo, C.I. Kim, Etch characteristics of HfO_2 thin films by using CF_4/Ar inductively coupled plasma, Vacuum 93 (2013) 50–55.
[33] I. Hotovy, S. Hascik, M. Gregor, V. Rahacek, M. Predanocy, A. Plecenik, Dry etching characteristics of TiO_2 thin films using inductively coupled plasma for gas sensing, Vacuum 107 (2014) 20–22.
[34] K.-R. Choi, J.-C. Woo, Y.-H. Joo, Y.-S. Chun, C.-I. Kim, Dry etching properties of TiO_2 thin films in O_2/CF_4/Ar plasma, Vacuum 92 (2013) 85–89.
[35] S. Tegen, P. Moll, Etch Characteristics of Al_2O_3 in ICP and MERIE Plasma Etchers, Journal of The Electrochemical Society 152 (4) (2005).
[36] J.Y. Choi, C.F. Ahles, Y. Cho, A. Anurag, K.T. Wong, S.D. Nemani, E. Yieh, A. C. Kummel, Selective pulsed chemical vapor deposition of water-free HfO_x on Si in preference to SiCOH and passivated SiO_2, Applied Surface Science 512 (2020), 145733.